ELSEVIER

Journal of Alloys and Compounds 419 (2006) 32–39

Journal of ALLOYS AND COMPOUNDS

www.elsevier.com/locate/jallcom

Synthesis and magnetic characterization of Ni nanoparticles and Ni nanoparticles in multiwalled carbon nanotubes

Daniele Gozzi [a,*], Alessandro Latini [a], Gustavo Capannelli [b], Fabio Canepa [c], Myrta Napoletano [c], Maria Roberta Cimberle [d], Matteo Tropeano [e]

[a] *Dipartimento di Chimica, Università di Roma La Sapienza, Piazzale Aldo Moro 5, 00185 Roma, Italy*
[b] *INSTM and Dipartimento di Chimica e Chimica Industriale, Via Dodecaneso 31, 16146 Genova, Italy*
[c] *INFM-LAMIA and Dipartimento di Chimica e Chimica Industriale, Via Dodecaneso 31, 16146 Genova, Italy*
[d] *CNR-IMEM Dipartimento di Fisica, Via Dodecaneso 33, 16146 Genova, Italy*
[e] *INFM-LAMIA, C. so Perrone, Genova, Italy*

Received 15 September 2005; received in revised form 10 October 2005; accepted 14 October 2005
Available online 21 November 2005

Abstract

Nickel nanoparticles were synthesized by reduction of nickel acetylacetonate in a monosurfactant system. These nanoparticles, mostly amorphous, were used as catalyst for the growth of multiwalled carbon nanotubes by the catalytic decomposition of methane at 500 °C. TEM analysis reveals a wide size distribution of the diameter of the particles centred around two main values. A detailed characterization of the magnetic properties of the Ni nanoparticles and Ni nanoparticles carbon nanotubes embedded is hereby presented. Both the systems show superparamagnetic behaviour above the blocking temperature T_B. Magnetization data are well fitted by an equation formed by two weighted Langevin functions and display the correct scaling of M/M_S versus H/T for superparamagnetic nanoparticles. The hysteresis loops obtained below T_B agree with the ferromagnetism of single-domain particles, confirmed also by the expected temperature dependence of the coercive field H_C. Differences in the coercive fields at increasing and decreasing applied magnetic fields are to be ascribed to a NiO layer originating an exchange bias with inner Ni. The smallness of the coercive fields difference (around 5 Oe) confirms that the used preparation method produces a very thin NiO layer around Ni nanoparticles.

PACS: 61.46.+w; 75.20.−g; 75.50.Tt

Keywords: Carbon nanotubes; Magnetic properties; Catalytically grown carbon

1. Introduction

The synthesis and chemico–physical characterization of elements as Fe, Co or Ni in nanometric scale is nowadays an important topic in materials science not only for their peculiar properties related to the reduced size but also for their relevance from a technological point of view. Possible potential applications of the nanostructured materials as catalysts (high value of the surface area), high-density magnetic recording media and medical diagnostics have been recently emphasized [1–3]. More recently [4], the use of composites with nano-sized ferromagnetic particles as absorbers of electromagnetic waves for technological applications starting from radar systems and silent rooms to wireless communications has been increased.

Different techniques have been adopted to obtain ferromagnetic elements with nanometric dimensions: arc discharge [5], evaporation [6], sputtering [7] and sonochemical method [8]. However, the high *surface to mass* ratio has the consequence to increase enormously the reactivity of the nanoparticles that could prevent their technological use. Therefore, the coating of these magnetic nanoparticles by protective layers or the synthesis of magnetic particles in carbon capsules has a particular interest since it can prevent any kind of reaction, particularly the oxidation, provided the temperature is kept close to the room temperature.

Finally, magnetic nanoparticles can be used as origin for the growth of carbon nanotubes. This is a new form of carbon configurationally equivalent to two-dimensional graphene sheet rolled into a tube and can offer amazing possibilities to create future

* Corresponding author. Tel.: +39 06 4991 3849; fax: +39 06 4991 3849.
E-mail address: Daniele.Gozzi@uniroma1.it (D. Gozzi).

0925-8388/$ – see front matter © 2005 Elsevier B.V. All rights reserved.
doi:10.1016/j.jallcom.2005.10.012

nanoelectronics devices, circuits, and computers through further circuitry integration.

We prepared either Ni nanoparticles, mostly in the amorphous state, and carbon nanotubes embedding Ni nanoparticles using the Ni nanoparticles as "seeds" for the growth of carbon nanotubes (randomly oriented). We present, here, the information obtained on these two systems by transmission electron microscopy (TEM) and magnetic measurements as well as some experimental evidences on the multiwalled carbon nanotubes, MWCNT, growth.

2. Experimental

Ni nanoparticles were synthesized according to the method developed by Hou and Gao [9], i.e., by reducing Ni acetylacetonate by $NaBH_4$ in a mono-surfactant system. The combustion and ICP (Ion Coupled Plasma) analyses of the product after centrifugation and vacuum drying gave the composition: $C = 5.8 \pm 0.3$; $H = 1.0 \pm 0.1$; $N = 0.4 \pm 0.1$; $Ni = 4.6 \pm 0.1$ and inorganic inert residuals up to 100. All the figures are given by wt.%. The catalyst for the growth of MWCNTs was prepared through a dispersion of the Ni nanoparticles over high surface area ($960 \pm 1\ m^2\ g^{-1}$) MCM-41 mesoporous silica. To do this 0.18371 g of the synthesized material, i.e., 0.0084 ± 0.0002 g of Ni nanoparticles were suspended in 30 ml of *n*-hexane and 0.55098 g of MCM-41 silica were soaked in the suspension under stirring at room temperature. The stirring was continued until the surfactant liquid became transparent. Then, the temperature was gently raised up to about 70 °C and kept constant until to the solvent full evaporation. The solid catalyst was recovered and dried under vacuum. Thus, the Ni nanoparticle concentration, c_{cat}, in the catalyst dispersion is 1.5 ± 0.4 wt.%.

The quantity, q, of 0.15548 g of Ni nanoparticle dispersion in MCM-41 silica was placed in a fixed bed catalytic micro reactor (Fig. 1). The catalyst was heated up to 500 °C at 300 °C/h in an Ar stream. When at 500 °C, Ar was substituted by CH_4 at 5 $cm^3\ min^{-1}$ at STP. The kinetics of reaction:

$$CH_4(g) \rightarrow C(nano) + 2H_2(g) \quad (1)$$

was monitored by a Balzers Quadstar© quadrupole mass spectrometer, QMS, operating in multiple ion detection, MID, mode. The admission of the reacted gas mixture into the QMS chamber was realized by a system (see Fig. 1) constituted by a stainless steel capillary (1 m long × 150 μm i.d.), a rough vacuum pumping and a dosimeter valve (Balzers UDV 040). The capillary was maintained at 150 °C and at fixed pressure gradient (1 bar rel. at the inlet and 1 mbar at the outlet). Methane utilized was 97.5% with 2.5% of H_2.

Because from preliminary experiments it was confirmed that only reaction (1) takes place, only amu corresponding to CH_4 (and its fragments CH_3, CH_2, CH, C) and H_2 were set for the MID detection. In order to establish, the time of the complete substitution of Ar with CH_4 also amu = 40 was added to the previous set.

After about 16.9 h from the Ar/CH_4 substitution, the reactor was cooled down to room temperature at 300 °C/h keeping still the same CH_4 flow-rate. The final mass gain, Δm, entirely attributable to the formation of MWCNTs, was 0.06347 g. The solid reaction product was recovered from the reactor, washed thoroughly with NaOH ~2 M to remove the silica support, then with deionised water and acetone and finally dried under vacuum. The combustion analysis of MWCNT recovered gave: $C = 95.4 \pm 0.3\%$, $H = 0.2 \pm 0.1\%$ and Ni up to 100, i.e., $c_{Ni} = 4.4 \pm 0.3\%$.

The structural investigation was carried out by means of transmission electron microscope (TEM) model JEOL JEM 2010 FEEM 200 KV from JEOL Ltd. The samples for TEM analysis were firstly finely dispersed in isopropanol and, then, exposed to ultrasonic vibrations to decrease the aggregation. The diameter distribution has been evaluated over more than 1000 particles. X′Pert Pro diffractometer by Philips, working at Cu Kα1 wavelength, was utilized for XRD analyses.

Magnetic measurements were performed using a Quantum Design SQUID MPMS magnetometer in the 5–350 K temperature range and in applied $\mu_0 H$ magnetic fields between ±5.5 Tesla (T). Additional magnetization measurements up to 9 T were obtained by a Maglab^{2000} equipment (extraction method) from Oxford Instruments Inc.

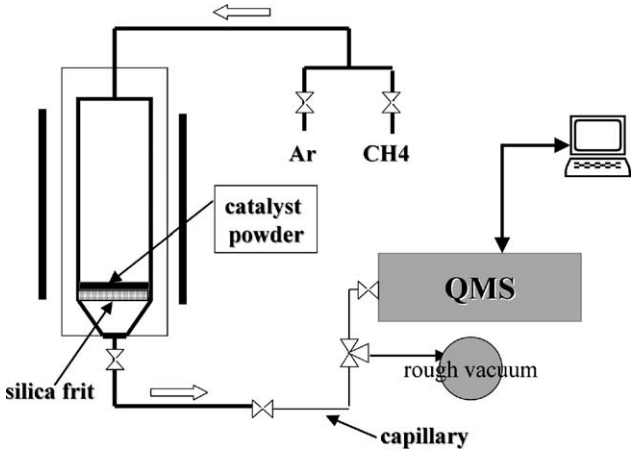

Fig. 1. Schematic view of the experimental assembly for MWCNT growth.

3. Results

3.1. Kinetics of MWCNT growth

The ionic intensities of the amu set acquired by the QMS is reported in Fig. 2. On the left scale are reported the amu of CH_4 (amu = 16) and its fragments as well as amu = 40, i.e., Ar. The ionic intensity of H_2 is reported on the right scale. The origin of the time scale is fixed at the time when the valve of Ar becomes off and the valve of CH_4 is opened (see Fig. 1). At the time origin the micro reactor is already at 500 °C. The time at which the catalyst *sees* CH_4 without Ar is the time corresponding to the disappearing of Ar signal. This occurs at time t^*. When the system is cooled down at room temperature, the rate of reaction (1) goes rapidly to zero and, accordingly, the ionic intensities related to methane and hydrogen change with opposite trends, as expected. The final ionic intensity of H_2 cannot be zero it being the main impurity of CH_4 used.

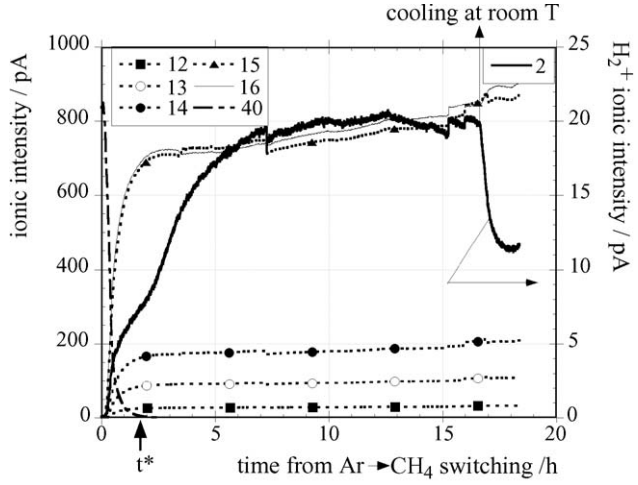

Fig. 2. Ionic intensities from QMS during the MWCNT growth. Time t^* is the time at which Ar is completely replaced by CH_4.

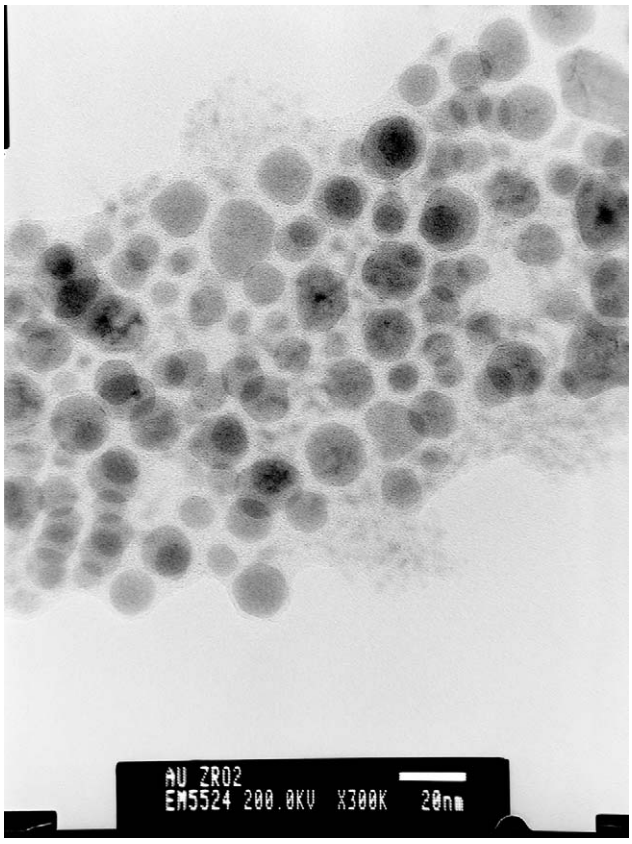

Fig. 3. TEM of Ni nanoparticle after preparation.

3.2. XRD and TEM

In Fig. 3, a typical HREM image of Ni nanoparticles is reported, while in Fig. 4 the size distribution histogram of the Ni nanoparticles is presented. This figure displays a wide distribution of particle diameters centered around two main values: about 70% of the particles has a diameter of about 5 nm, while only about 25–30% of the particles present a diameter between 10 and 20 nm. This bimodal distribution has been fitted with a double Gaussian function, reported as dot line in the same Fig. 4: we obtain two mean diameters of the particles, namely $d_1 = 4.6$ nm and $d_2 = 15.4$ nm.

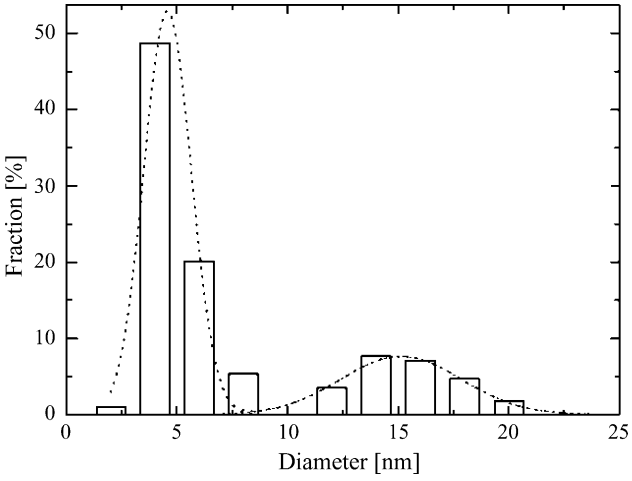

Fig. 4. Size distribution histogram of Ni nanoparticles as obtained from the TEM analysis.

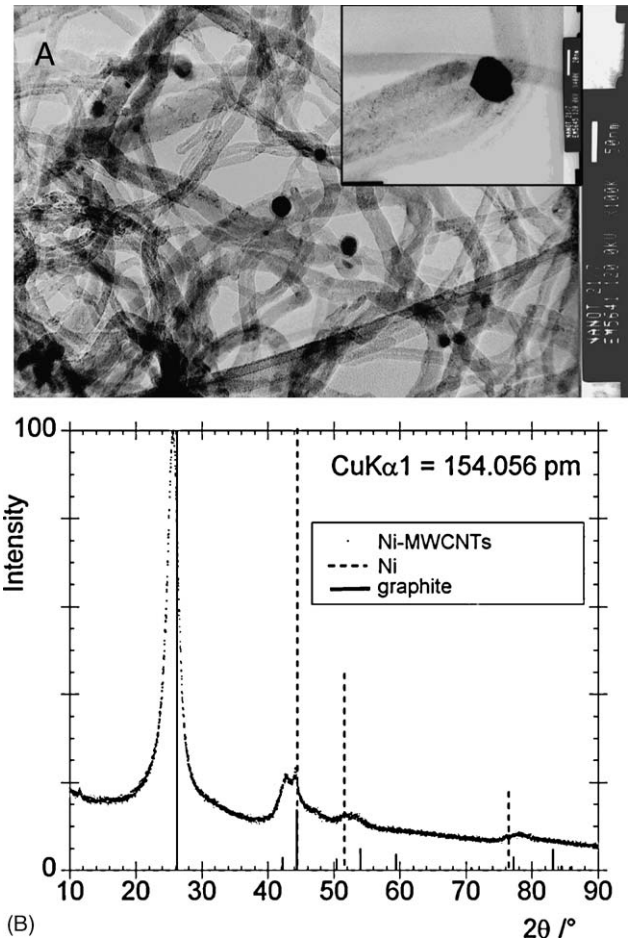

Fig. 5. (A) TEM micrograph of MWCNTs with Ni nanoparticle embedded. A tip shape nanoparticle attached to a MWCNT is shown in the inset. (B) XRD spectrum of Ni-MWCNTs at Cu Kα1 radiation. Lines of a reference graphite syn and fcc Ni are from PCPDFWIN version 2.2, June 2001 data base (ICPDS-ICDD), respectively, #87-0712 and #75-1621.

The XRD spectrum of the Ni nanoparticles displays no peaks originating from the face-centred cubic (fcc) Ni structures showing that a great part of Ni is in the amorphous state. Only peaks due to the inert inorganic residuals coming from the synthesis appear.

Ni nanoparticles embedded in MWCNTs are shown in Fig. 5A. Each MWCNT carries at one of its ends a Ni nanoparticle. The analysis of the distribution of Ni nanoparticles in MWCNTs, not reported here, gives the same bimodal result. Differently from the Ni nanoparticles, the XRD spectrum of Ni-MWCNTs, reported in Fig. 5B, shows clearly the fcc features of the Ni nanoparticles linked to MWCNTs, as well as the typical finger print of a hexagonal graphite structure. The comparison with one of the closest spectra reported in the ICPDS data base gives the indication that the graphene planes in MWCNTs, d_{002} spacing, are separated 75 pm more than graphite assumed as reference. The presence of Ni features that appear as weak signals, because Ni concentration is low, but in the expected intensity

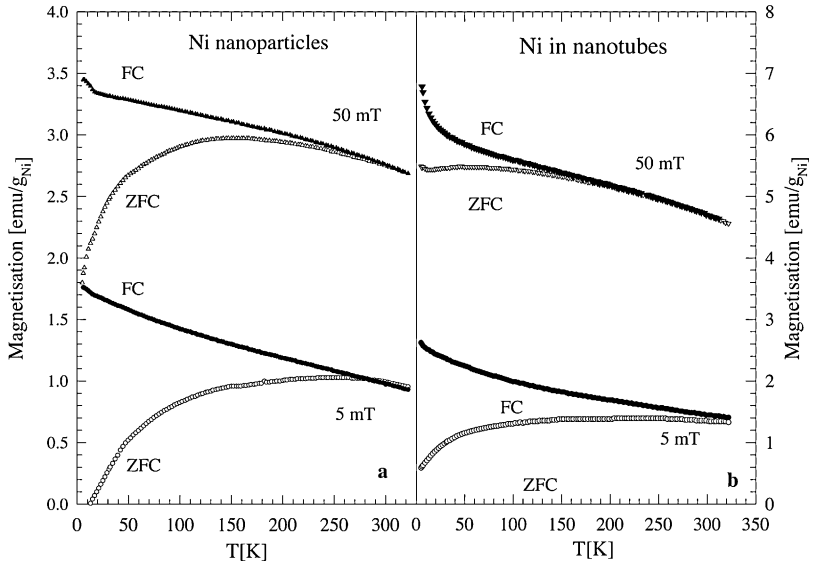

Fig. 6. Temperature dependence of the magnetization of: (a) Ni nanoparticles and (b) Ni nanoparticles in MWCNT obtained at 5 and 50 mT.

pattern, confirms that the transition amorphous/crystalline at the temperature of the CH_4 decomposition has been promoted during the heating of the Ni nanoparticles. The absence of no preferential orientation suggests that transition leads only to polycrystalline nanoparticles.

3.3. Magnetic measurements

Fig. 6 shows the temperature dependence of the magnetization between 5 and 300 K of the Ni nanoparticles (a) and Ni nanoparticles in carbon nanotubes (b), respectively. The data were taken in zero-field-cooling (ZFC) and field-cooling (FC) conditions at two different applied magnetic fields, i.e., 5 and 50 mT. ZFC and FC curves show a bifurcation that decreases at increasing magnetic fields. Furthermore, the ZFC curves show a large decrease of the magnetization: this decrease, quite evident in Ni nanoparticles, is less strong in nano Ni in MWCNT (note in Fig. 6, the behaviour of ZFC curve at 50 mT where the magnetization is nearly constant below the bifurcation point). This last behaviour may be due to weak magnetic interactions in the system as we will discuss in the following. We observe also that the magnetization values for Ni nanoparticles are lower with respect to the values of nano Ni in MWCNT in the same field and temperature conditions.

In the low temperature regime, the Ni nanoparticles and Ni nanoparticles in MWCNT show hysteretic behaviour like ferromagnetic systems: the hysteresis loops at different temperatures have been performed after a ZFC procedure and with a thin field span ($\leq$1 mT) up to 0.011 T. They are presented in Fig. 7a and b, respectively. For Ni nanoparticles, we observe hysteresis loops decreasing at increasing temperature with relatively low values of the magnetization (4 emu/g_{Ni} at 0.2 T and 5 K). Once closed, the magnetization doesn't saturate, but increases continuously with a slope, which depends on the applied temperature. On the contrary, Ni nanoparticles in MWCNT display larger hysteresis loops saturating at relatively high values (12 emu/g_{Ni} at 0.4 T

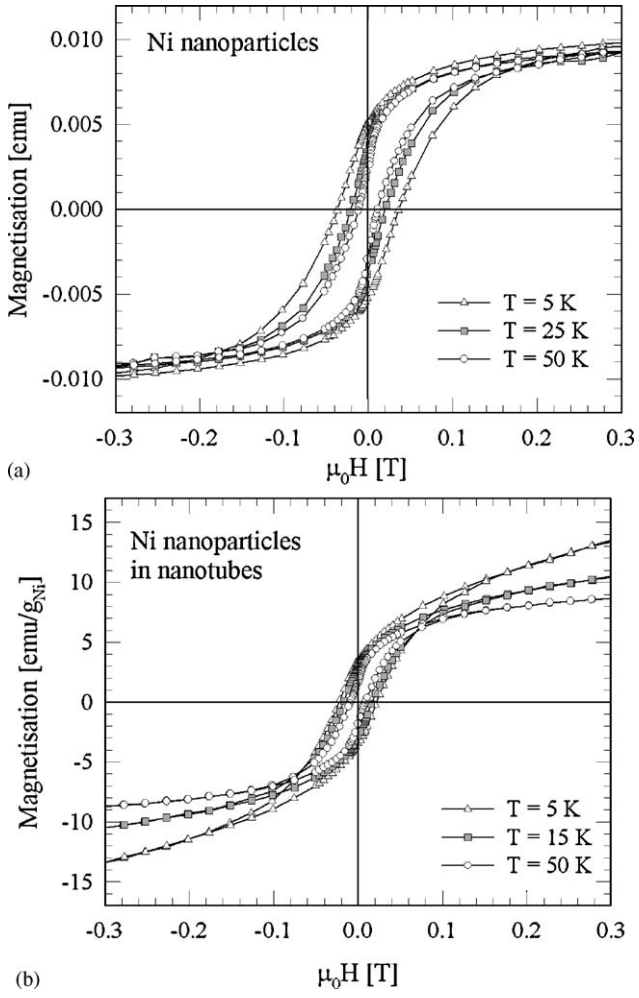

Fig. 7. Magnetization loops of: (a) Ni nanoparticles and (b) Ni nanoparticles in MWCNT at selected temperatures.

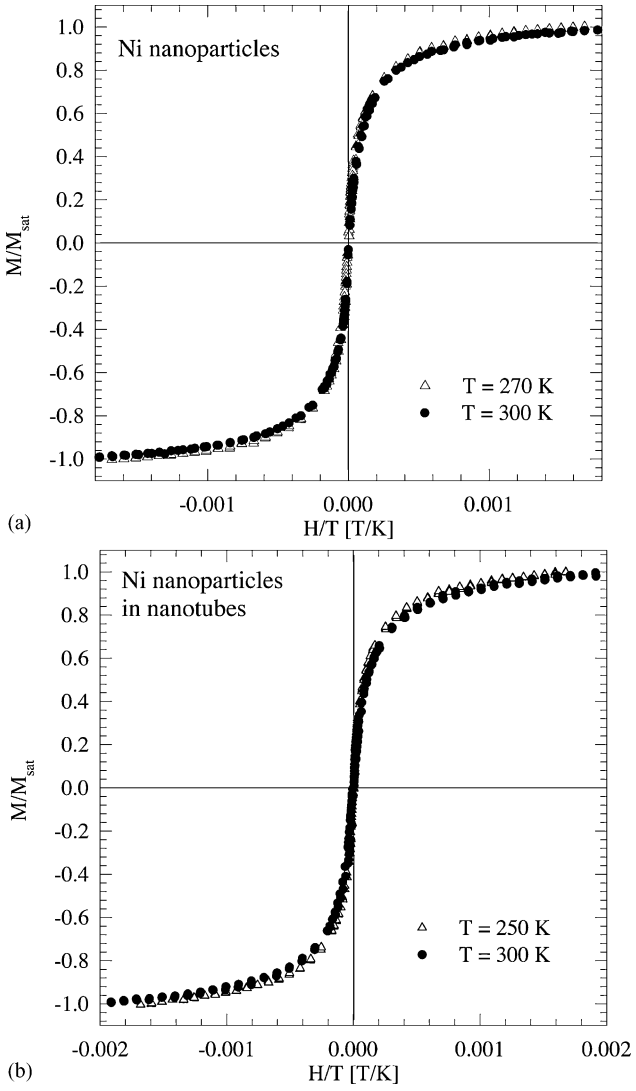

Fig. 8. Normalized magnetization (M/M_S) as a function of H/T for Ni nanoparticles (a) at $T = 270$, 300 K and for Ni nanoparticles in MWCNT (b) at $T = 250$, 300 K. For both plots, the solid line is the fit with a weighted sum of two Langevin functions, as described in the text.

and 5 K) and showing no temperature dependence. Also, the remanent magnetization (M_R) and the coercive field (H_C) are larger for nano Ni in MWCNT with respect to Ni nanoparticles in the same temperature conditions.

High temperature magnetization data normalized to the saturation magnetization M_S, are reported as a function of the H/T ratio together with the Langevin fit of the data in Fig. 8a and b, respectively.

4. Discussion

4.1. MWCNT growth

Assuming that the observed experimental curves reported in Fig. 2 are only due to reaction (1), the growth rate of MWCNT would be simple proportional to the ionic intensity of H_2. This is true even if being approximate in order to evaluate correctly the amount of CH_4 converted in MWCNT. Therefore, some facts should be taken into account: (i) constant response uncertainty of QMS on long times especially when considering low ionic intensity values like that in the case of H_2; (ii) H_2 is already present in CH_4; (iii) variable composition occurring before t^*. In the previous reasoning, we assumed that all carbon produced grows as MWCNTs. This agrees well with TEM analysis. Therefore, to evaluate quantitatively the conversion, η, of methane in MWCNT, equation below has been used:

$$\eta = \left(\frac{i_{H_2}/2f_{H_2}}{\sum_0^4 i_{CH_i}/f_{CH_i} + i_{H_2}/2f_{H_2}} \times 100 \right)_T - \left(\frac{i_{H_2}/2f_{H_2}}{\sum_0^4 i_{CH_i}/f_{CH_i} + i_{H_2}/2f_{H_2}} \times 100 \right)_{T_{room}} \quad (2)$$

where i and f stand, respectively, for ionic intensity and calibration factor. The second term on the right side of Eq. (2) represents the apparent conversion at room temperature due to the H_2 content in the feeding methane. The summation is extended to all the ionic species of CH_4 measured by QMS. Data calculated through Eq. (2) are plotted in Fig. 9. By comparing Fig. 9 with Fig. 2, it appears clear that there is a time interval, after t^*, and lasting until t_0, during which the slope of i_{H_2} decreases. This could be attributed to some consumption of H_2 by the catalyst. At this stage, it is difficult to establish the real process or processes occurring. It is reasonable to associate this phenomenon to both the reduction of some NiO, coating the Ni nanoparticles, and chemisorption and/or absorption of H_2 by the nanoparticles themselves.

The ratio, γ, between the weight, w, of Ni consumed by the embedding in MWCNTs and quantity, w_0, of Ni in the catalyst dispersion q is given by:

$$\gamma = \frac{w}{w_0} = \frac{c_{Ni}\Delta m}{c_{cat} q} \leq 1 \quad (3)$$

In the present experiment, $\gamma = 1.2 \pm 0.5$. The large value of the error comes from the calculation of the absolute maximum error using the respective errors on c_{Ni} and c_{cat}. In practice, γ can be considered close to 1. This leads at least two considerations: (a)

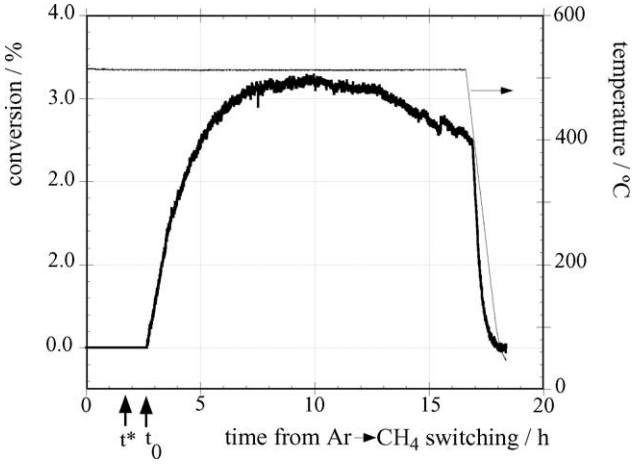

Fig. 9. Conversion of methane in MWCNT as function of time.

practically, all the Ni nanoparticles into the MCM-41 dispersion are suitable to allow the growth of MWCNT. In fact, looking at Fig. 9, it appears clear that before stopping the reaction the rate of CH_4 conversion, i.e., MWCNT formation rate, is already decreasing; (b) in contrast, the low value of η indicates that a large number of preferential paths are expected to be formed in the catalytic bed of the microreactor due to the high specific volume of MWCNT produced during the reaction progress.

It has been shown [10] that using a catalyst of different chemical nature and micrometer sized, MWCNT growth occurs on self-generated tip-shaped single crystal nanoparticles. In the present case, looking at Fig. 5, it appears clear that most of the Ni nanoparticles are round shaped except for a few exceptions as reported in the inset of same Fig. 5. As stated before (see Section 3.2), no evidence here exists that a MWCNT grows on a single crystal catalyst nanoparticle. It could be inferred that a different growth mechanism is at working here though the main chemical process (CH_4 catalytic decomposition) and experimental conditions are exactly the same.

4.2. The low T magnetic properties of Ni nanoparticles and nano Ni in MWCNT

The starting point for the analysis of the magnetic properties of the two systems, i.e., Ni nanoparticles and nano Ni in carbon nanotubes, is the observation of their common superparamagnetic behaviour in addition to the analysis of the magnetic differences between crystalline and amorphous magnetic nanoparticles.

Magnetic nanoparticles behave like *single domain* particles depending on the size of the particle: on the basis of the magnetic domain theory [11,12], the critical radius is strongly related to the saturation magnetization of the material, its exchange constant and anisotropy constant. So, it is possible to calculate it and for Ni the value is $R_C = 21.3$ nm. In the amorphous state, a magnetic nanoparticle behaves like a perfect superparamagnet at all temperatures: no hysteresis cycle is observed nor a saturation value at high-applied magnetic fields [13].

The hypothesis that our Ni nanoparticles are mainly formed by amorphous particles is suggested by the absence of Ni peaks in the XRD measurements and it was also confirmed by other experimental evidences. The hysteresis cycle at 5 K up to 9 T is displayed in Fig. 10. At very low fields, we have a sharp increase due to the crystalline fraction of the Ni nanoparticles, which behaves like a ferromagnet. The continuous increase of the magnetization above 0.2 T is the superparamagnetic behaviour of the amorphous Ni. It should be pointed out that also at 9 T the saturation limit is not reached, as expected for a pure superparamagnet.

This hypothesis explains also the hysteresis cycle behaviours of Ni nanoparticles presented in Fig. 7a. The hysteresis cycle is due to the small fraction of crystalline Ni nanoparticles and the continuous increase of the magnetization after the cycle is due to the rotation of the magnetic moments of the amorphous Ni towards the applied field: this rotation is more effective at lower temperatures due to the lower thermal energy opposing to the magnetic field effect. Ni nanoparticles in MWCNTs (see

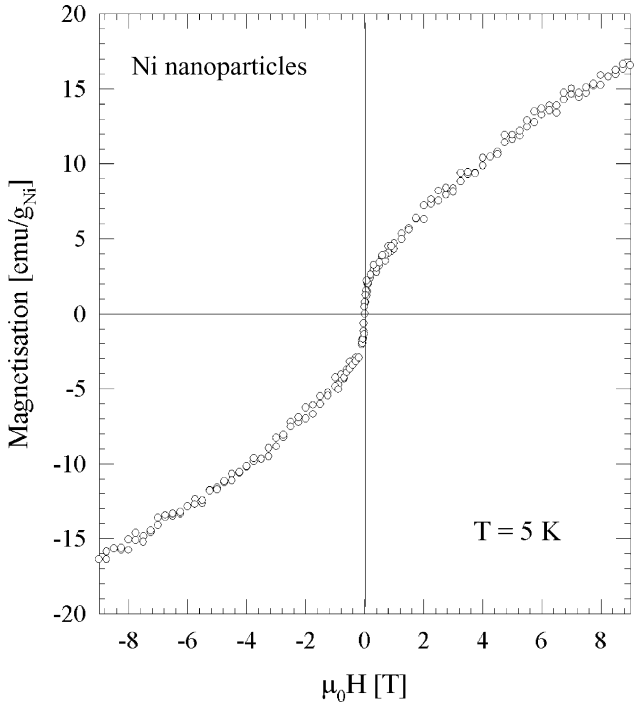

Fig. 10. High field hysteresis loop of Ni nanoparticles at 5 K.

Fig. 7b), on the contrary, below the blocking temperature, behave like a ferromagnetic system: a saturation is reached and the temperature has low or null effect.

A small difference between H_{C-} and H_{C+}, i.e., the coercive fields obtained with decreasing and increasing applied magnetic fields, is observed in both systems at all the measured temperatures. This difference may be attributed to the existence of a very narrow NiO layer around the Ni particle, which can create an exchange bias between ferromagnetic Ni and antiferromagnetic NiO [14]. In our case, the smallness of $\Delta H_C = (H_{C+} + H_{C-})/2$ (around 5 Oe) suggests that the synthesis here adopted has the result to prepare metallic nanoparticles less oxidized with respect to other preparation routes also in comparison with other results [15].

From the theory of superparamagnetism, it is possible to obtain the blocking temperature from the temperature dependence of the coercive field using the equation [14,16]:

$$H_C = H_{C0}\left[1 - \left(\frac{T}{T_B}\right)^{1/2}\right] \quad (4)$$

where H_{C0} is the coercivity at 0 K.

The expected low temperature linear dependence of the coercive fields with respect to the root of the temperature is presented for Ni nanoparticles in nanotubes in Fig. 11 while in the inset the data for Ni nanoparticles are reported. From these data, one could obtain the blocking temperatures $T_B = 74$ and 68 K, for Ni nanoparticles and nano Ni in MWCNT, respectively. We remark anyway that these temperature values are meaningless since in systems where a size distribution of the nanoparticles is present, a distribution of the blocking temperatures is expected, being T_B proportional to the volume of the nanoparticle through the

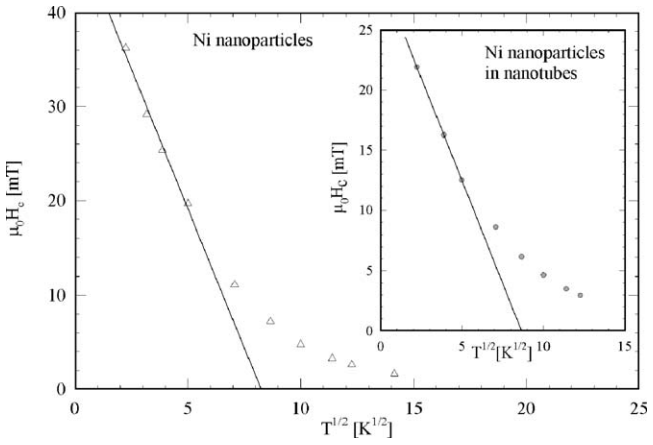

Fig. 11. Linear dependence of the coercivity H_C for Ni nanoparticles in MWCNT with respect to $T^{1/2}$. In the inset, the same linear dependence is reported for Ni nanoparticles.

relation:

$$T_B = \frac{K\langle V\rangle}{25k_B} \tag{5}$$

where K is the magnetic anisotropy energy per unit volume.

So, by using the bimodal size distribution obtained by TEM analysis, we have calculated the T_B values corresponding to the two mean size values of the Ni nanoparticles in MWCNT: in this case, the crystallization of the nickel ($T_{cr} = 333\,^{\circ}C$) [17] is complete due to the higher working temperature applied for the synthesis of the nanotubes (500 °C). By the relationships:

$$T_B(H_C) = 0.72\langle T_{B1}\rangle + 0.28\langle T_{B2}\rangle,$$
$$\frac{\langle T_{B1}\rangle}{\langle T_{B2}\rangle} = \frac{\langle V_1\rangle}{\langle V_2\rangle} = \left(\frac{\langle r_1\rangle}{\langle r_2\rangle}\right)^3 = 0.0266 \tag{6}$$

where $T_B(H_C)$ is the blocking temperature obtained from the fit of Fig. 11, r_1 and r_2 are the mean radii of the bimodal distribution obtained from TEM and coefficients 0.72 and 0.28 are the weights of the two types of nanoparticles obtained from the integration of the areas of the two peaks reported in the histogram of Fig. 4. The calculated two different mean blocking temperatures are: $\langle T_{B1}\rangle = 6$ K and $\langle T_{B2}\rangle = 230$ K. This analysis, showing the existence of a high blocking temperature, explains why the merging of the ZFC and FC curves, that must happens at T_B, is observed above $T = 200$ K.

Finally, from Eq. (4), we obtain $H_{C0(1)} = 29$ mT for Ni nanoparticles and $H_{C0(2)} = 48$ mT for Ni in MWCNT. It should be noted that both values are well below the value of 95 mT obtained from the equation:

$$H_{C0} = 0.64\frac{K_1}{M_S} \tag{7}$$

for randomly oriented and non interacting particles, using the saturation magnetization $M_S = 541$ emu/cm^3 and taking for the anisotropy constant K_1 the low temperature value ($K_1 = -8 \times 10^5$ erg/cm^3). Weak magnetic interactions could decrease the H_{C0}. In our case, the H_{C0} calculation is affected by the wide size and blocking temperature distributions hindering any further analysis.

4.3. The high T magnetic properties of Ni nanoparticles and nano Ni in MWCNT

In the theory of superparamagnetism, the magnetization follows the Langevin function:

$$\frac{M}{M_S} = \coth\left(\frac{\mu H}{k_B T}\right) - \frac{k_B T}{\mu H} \tag{8}$$

where M_S is the saturation magnetization, H the magnetic field, k_B the Boltzmann constant, T the temperature and μ is the average magnetic moment of the nanoparticles.

The fit of both our magnetic data with a single Langevin function was, anyway, disappointing. In fact, the wide distribution of particle sizes in our samples resulting in a distribution of magnetic moments requires the use of a weighted sum of Langevin functions [18] or at least the sum of two Langevin function related to the bimodal size distribution function observed in our samples [19]. In such way, a good fit of the magnetization in the whole field range was obtained and the results of the fit are shown, as solid line, in Fig. 8a and b for Ni nanoparticles and nano Ni in MWCNT, respectively.

For Ni nanoparticles, we find from the fit that 71% of our particles carry a mean magnetic moment $\mu_1 = 17\,000\mu_B$ while for 29% the mean magnetic moment μ_2 is $150\,000\mu_B$. Since the experimental magnetic moment of the single particle is related to the volume of the particle by the following equation:

$$\mu = M_S\langle V\rangle \tag{9}$$

where M_S is the saturation magnetization of bulk nickel, our values are consistent, under the hypothesis of spherical shape of the particles, with diameters of $r_1 = 4.2$ nm and $r_2 = 8.8$ nm, respectively.

On the other hand, for Ni nanoparticles in nanotubes, we obtain a similar distribution of the two magnetic moments and hence of the dimensions: around 76% of Ni nanoparticles in nanotubes have $\mu_1 = 16\,000\mu_B$ and 24% have $\mu_2 = 150\,000\mu_B$. These values lead to $r_1 = 4.1$ nm and $r_2 = 8.8$ nm.

In both the systems, a good agreement with the TEM results, i.e., the mean radius value and the percentage, is obtained from the Langevin fit.

5. Conclusions

The present work belongs to a research program oriented to functionalise CNTs by single or polycrystalline metallic or intermetallic nanoparticles that have by themselves relevant physical and/or chemical properties such as electrical, electronic, magnetic, catalytic, piezoelectric and so on. The first objective is to check if and how the CNTs change their properties or the changes are only at expenses of the embedded nanoparticles. Next step is to envisage and test some specific application in the field of the nanotechnologies.

The main difficulty encountered in the present work is the preparation of uniform size and full crystalline Ni nanoparticles. Work is in progress to improve the method by selecting different reaction environments as well as the choice of the most appropriate working temperature.

The magnetic characterization of these materials reveals interesting features in these two systems. The superparamagnetic behaviour at high temperatures has been well analysed in terms of sum of two weighted Langevin functions in very good agreement with TEM results: the experimental data show similar dimensions of the Ni particles free and in carbon nanotubes. The very low evidence of NiO on the surface of the particles confirms the correctness of the synthesis route. The low temperature behaviour gives evidence of stronger ferromagnetic interactions among Ni nanoparticles in MWCNT with respect to Ni nanoparticles alone: the hysteresis loops are larger and the remanence and coercive fields are higher. In this way, it seems stimulating the preparation and the study of nanoparticles more ferromagnetic in carbon nanotubes, as for example, Sm_2Co_{17} or $Nd_2Fe_{14}B$.

Acknowledgements

Two of the authors (DG, FC) wish to thank the Ministero Istruzione, Università e Ricerca (MIUR) for the supported research PRIN2004 “Caratterizzazione Chimico fisica di composti intermetallici in forma di bulk e in forma di film”.

References

[1] L. Lu, M.L. Sui, K. Lu, Science 287 (5457) (2000) 1463–1466.
[2] H. Gleiter, Nanostruct. Mater. 1 (1) (1992) 1–19.
[3] J.H. Scott, S.A. Majetich, Phys. Rev. B 52 (17) (1995) 12564–12571.
[4] V.B. Bregar, IEEE Trans. Magn. 40 (3) (2004) 1679–1684.
[5] E.M. Brunsman, R. Sutton, E. Bortz, S. Kirkpatrick, K. Midelfort, J. Williams, et al., J. Appl. Phys. 75 (10, Pt. 2A) (1994) 5882–5884.
[6] T. Hayashi, T. Ohno, S. Yatsuya, R. Ueda, Jpn. J. Appl. Phys. 16 (5) (1977) 705–717.
[7] A. Gavrin, C.L. Chen, J. Appl. Phys. 73 (10, Pt. 2) (1993) 6949–6951.
[8] K.V.P.M. Shafi, A. Gedanken, R.B. Goldfarb, I. Felner, J. Appl. Phys. 81 (10) (1997) 6901–6905.
[9] Y. Hou, S. Gao, J. Mater. Chem. 13 (7) (2003) 1510–1512.
[10] D. Gozzi, A. Latini, Simultaneous production of molecular hydrogen and carbon nanotubes, Università di Roma “La Sapienza”. International Patent Pending PCT/IT2005/000587.
[11] C. Kittel, Phys. Rev. 70 (1946) 965–9671.
[12] W. Gong, H. Li, Z. Zhao, J. Chen, J. Appl. Phys. 69 (8, Pt. 2A) (1991) 5119–5121.
[13] F.E. Luborsky, in: E.P. Wohlfarth (Ed.), Ferromagnetic Materials, vol. 1, North Holland Publ., Amsterdam, 1980, p. 451.
[14] B.D. Cullity, in: Introduction to Magnetic Materials, Series in Metallurgy and Materials, Addison-Wesley, Reading, MA, 1972.
[15] Y.D. Yao, Y.Y. Chen, M.F. Tai, D.H. Wang, H.M. Ling, Mater. Sci. Eng. A 217/218 (1996) 281–285.
[16] B.H. Sohn, R.E. Choen, G.C. Papacfthymiou, J. Magn. Magn. Mater. 182 (1/2) (1998) 216–224.
[17] Yu Koltypin, G. Katabi, X. Cao, R. Prozorov, A. Gedanken, J. Non-Crystall. Solid 201 (1/2) (1996) 159–162.
[18] M. Solzi, M. Ghidini, G. Asti, in: H.S. Nalwa (Ed.), Magnetic Nanostructures, vol. 4, American Sci. Publ., 1972 (Chapter 4).
[19] V. Franco, A. Conde, J. Magn. Magn. Mater. 277 (1/2) (2004) 181–186.